

Space and phase resolved ion energy and angular distributions in single- and dual-frequency capacitively coupled plasmas

Yiting Zhang^{a)} and Mark J. Kushner^{b)}

Department of Electrical Engineering and Computer Science, University of Michigan, 1301 Beal Ave., Ann Arbor, Michigan 48109-2122

Nathaniel Moore,^{c)} Patrick Pribyl,^{d)} and Walter Gekelman^{e)}

Department of Physics, University of California, Los Angeles, California 90095

(Received 30 June 2013; accepted 9 September 2013; published 1 October 2013)

The control of ion energy and angular distributions (IEADs) is critically important for anisotropic etching or deposition in microelectronic fabrication processes. With single frequency capacitively coupled plasmas (CCPs), the narrowing in angle and spread in energy of ions as they cross the sheath are definable functions of frequency, sheath width, and mean free path. With increases in wafer size, single frequency CCPs are finding difficulty in meeting the requirement of simultaneously controlling plasma densities, ion fluxes, and ion energies. Dual-frequency CCPs are being investigated to provide this flexible control. The high frequency (HF) is intended to control the plasma density and ion fluxes, while the ion energies are intended to be controlled by the low frequency (LF). However, recent research has shown that the LF can also influence the magnitude of ion fluxes and that IEADs are determined by both frequencies. Hence, separate control of fluxes and IEADs is complex. In this paper, results from a two-dimensional computational investigation of Ar/O₂ plasma properties in an industrial reactor are discussed. The IEADs are tracked as a function of height above the substrate and phase within the rf cycles from the bulk plasma to the presheath and through the sheath with the goal of providing insights to this complexity. Comparison is made to laser-induced fluorescence experiments. The authors found that the ratios of HF/LF voltage and driving frequency are critical parameters in determining the shape of the IEADs, both during the transit of the ion through the sheath and when ions are incident onto the substrate. To the degree that contributions from the HF can modify plasma density, sheath potential, and sheath thickness, this may provide additional control for the IEADs. © 2013 American Vacuum Society. [<http://dx.doi.org/10.1116/1.4822100>]

I. INTRODUCTION

The use of low pressure plasmas in microelectronics fabrication is essential to maintaining critical dimensions (CDs) through anisotropic etching and conformal deposition. In this regard, controlling the ion energy and angular distributions (IEADs) incident onto the wafer is an important consideration for tuning CDs and optimizing selectivity.^{1,2} Although conventional capacitively coupled plasma (CCP) reactors powered by a single frequency (typically 10–20 MHz) meet many plasma processing requirements, more precise and separate control of both ion bombardment energies, and magnitudes of radical and ion fluxes are often desired.³ In an effort toward optimizing etch processes, multifrequency CCPs have been developed.^{4–6} A low frequency (LF) is intended to control the shape of the IEAD, whereas a high frequency (HF) is intended to control the production of ions and radicals. Typically, the LF is a few megahertz to 10 MHz and the HF is in the range from tens of MHz to as much as 100–200 MHz. Since the plasma represents a

nonlinear impedance, decoupling the mutual influence of the two frequencies often requires that the separation in frequency be at least tens of megahertz.⁶ Even with significant separation, recent studies have shown mutual interactions between the frequencies—that is, the IEADs are not unique functions of LF and the plasma density is not a unique function of HF.^{7,8}

Acknowledging the complexity of radio frequency (rf) sheath dynamics in dual frequency CCPs, many analytical, computational, and experimental efforts have addressed the shape of the IEAD delivered to the substrate.^{9–13} Both pulsing and nonsinusoid waveforms have been used to customize IEADs with good agreement between experiments and models.^{14,15}

Metze *et al.*,¹⁶ Kawamura *et al.*,¹ and others have analyzed ion energy distributions (IEDs) in a collisionless rf sheath in different frequency regimes. They found that the critical parameter determining the shape of the IEDs is τ_{ion}/τ_{rf} , where τ_{ion} is the transit time through the sheath and τ_{rf} is the rf period. In the LF regime ($\tau_{ion}/\tau_{rf} \ll 1$), the ions respond to the instantaneous electric field, and they reach the substrate with an energy nearly equal to the instantaneous sheath potential upon entering the sheath. Averaging over the rf period, the IED is broad and bimodal having a high energy (E_1) and low energy (E_2) peak. The separation between peaks, $\Delta E = E_1 - E_2$, approaches the maximum sheath potential

^{a)}Electronic mail: yitingz@umich.edu

^{b)}Author to whom correspondence should be addressed; electronic mail: mjkush@umich.edu

^{c)}Electronic mail: moore@physics.ucla.edu

^{d)}Electronic mail: pribyl@ucla.edu

^{e)}Electronic mail: gekelman@physics.ucla.edu

during the rf period. In the HF regime ($\tau_{\text{ion}}/\tau_{\text{rf}} \gg 1$), the ions take many rf cycles to cross the sheath, and they strike the wafer with the average sheath potential. The phase of the rf cycle at which the ions enter the sheath and the instantaneous sheath voltage at that instant are not particularly important. Starting at LF, with increasing $\tau_{\text{ion}}/\tau_{\text{rf}}$, ΔE shrinks until the two peaks cannot be resolved. Theory and experiments have shown that the ΔE is centered at the mean sheath voltage drop and depends on the ion mass ($\Delta E \sim m_{\text{ion}}^{-1/2}$).²

In the intermediate frequency regime ($\tau_{\text{ion}}/\tau_{\text{rf}} \approx 1$), inertia results in the ions partially responding to the time variation of the sheath potential, and obtaining analytic representations of the IEDs is difficult. A kinetic approach based using some form of Monte Carlo or particle in cell (PIC) simulations is typically used to obtain IEDs in this intermediate regime and for dual-frequency CCPs in particular.⁹

Georgieva *et al.*³ performed one-dimensional PIC modeling of both single and dual-frequency CCPs in Ar, CF₄ and N₂ mixtures at a pressure of 30 mTorr. The IED was narrow with one outstanding peak in the single frequency (13.56 MHz) case, whereas the IED became wide and bimodal in the dual-frequency (2 + 27 MHz) case. When the high frequency is applied, the electron density and consequently the sheath width oscillate at the HF within the LF cycle. This oscillation in sheath width, in addition to the additional HF voltage, is reflected in the IEDs. There is also evidence of electron and negative ion accumulation in the sheath during the anodic portion of the LF cycle, which additionally thins the sheath. In experiments performed by Schulze *et al.*,^{7,17} rapid oscillations of the sheath thickness were also observed in a dual-frequency (2 and 27.12 MHz) CCP using a He/O₂ gas mixture at 490 mTorr. During this oscillation, the maximum electron energy gain from stochastic heating can be expected around the minimum voltage of the LF component when the sheath edge is close to the electrode. An additional energy gain and increased excitation can be observed at the maximum sheath extension. The strong dual-frequency coupling brings about these complex electron dynamics within the sheath.

One conclusion of these works is that the HF has an important (or at least non-negligible) effect on the IEAD delivered to the substrate. An implied conclusion of these works is that as long as the HF is used to produce the plasma, the shape of the IEAD cannot be truly independent of plasma production.⁸ Since the sheath thickness is then a function of power deposition, there are second order effects that shape the IEAD, particularly at higher pressures where the sheath may become collisional.

These interdependencies motivate examining low pressure (a few mTorr) inductively coupled plasmas (ICPs) having multiple frequencies applied to the substrate.¹⁸ In these systems, the plasma production is more nearly a unique function of the ICP power and the sheath is essentially collisionless. The LF and HF biases can be independently varied without significantly affecting ion or radical production.

The majority of studies to date have emphasized the shape of the IEADs when the ions strike the substrate since this is the quantity that directly affects the feature in microelectronics

fabrication. The final shape of the IEAD is the end result of the transit of ions from the bulk plasma, through the presheath and through the sheath. To better understand the dynamics of IEADs as they strike the substrate, it is instructive to track the formation of the IEAD as ions transit from the bulk plasma to the wafer. Experimentally, this investigation may be conducted using laser-induced fluorescence (LIF), which is capable of measuring components of the ion velocity distributions (IVDs) as a function of position in the sheath and phase during the rf cycle.^{19–23} For example, Jacobs *et al.* have used LIF to measure IVDs in a pulsed ICP reactor.²⁴ They observed ions approaching the Bohm velocity entering the sheath. They also applied this technique to tracking ions transiting a 2.2 MHz rf biased sheath as a function of phase. The phase resolved IVDs vary dramatically throughout the cycle, in accordance with theory.²⁵

In this paper, we report on a computational investigation of the time and spatial development of IEADs in low pressure ICPs having single and multifrequency substrate biases as the ions transit from the bulk plasma, through the presheath and sheath, and are incident onto the substrate. The choices of geometry, biasing pressure, and gas mixture were made to enable comparison to a companion experimental investigation of IVDs in the sheath as a function of phase using LIF. The simulations were performed with an ion Monte Carlo Simulation embedded within the Hybrid Plasma Equipment Model (HPEM), which is described in Sec. II. IEADs for single frequencies applied on the substrate while varying frequency and pressure, and comparison to experiment, are discussed in Sec. III. IEADs for dual frequency excitation are discussed Sec. IV. Our concluding remarks are in Sec. V.

II. DESCRIPTION OF THE MODEL

The HPEM used in this study is a two-dimensional fluid-hybrid plasma equipment model which has been previously discussed in detail.²⁶ HPEM uses a hierarchical approach in which modules addressing different physical processes exchange information on different time scales. The modules used in this study are the electromagnetic module (EMM) in which the wave equation is solved for the inductively coupled electric fields, the electron energy transport module (EETM) in which energetic secondary electrons accelerated by sheaths are tracked using a Monte Carlo simulation, and the fluid kinetics module (FKM) in which densities, fluxes, and energies of species are obtained, as well as obtaining the electric potential by solving Poisson's equation. The electron temperature is obtained by solving the electron energy conservation equation with transport coefficients provided by stationary solutions of Boltzmann's equations with sources from energetic secondary electrons provided by the EETM. Finally, the plasma chemistry Monte Carlo module (PCMCM) is used to obtain the ion trajectories from the bulk plasma through the time-varying sheath.

Operationally, on each iteration through the modules, the EMM computes the inductively coupled electric and magnetic fields and passes these values to the EETM, which

produces the electron impact source terms resulting from secondary electron emission and transport. The output of EMM and EETM are transferred to FKM in which the plasma transport equations are integrated for $0.5 \mu\text{s}$. Continuity, momentum, and energy equations are solved for all heavy particles (neutrals and ions). Continuity and energy equations are solved for electrons while assuming that fluxes are given by the Scharfetter–Gummel expression, which captures upwind-and-downwind properties in a drift-diffusion formulation. Poisson's equation is solved using a semi-implicit technique. At the end of this period of time integration, electric fields, conductivities, and densities are transferred to the EMM and EETM. The electric fields are recorded as a function of phase over the LF cycle with sufficient resolution to capture the HF dynamics. These space and phase dependent electric fields are then interpolated during the EETM to advance particle trajectories. The process is repeated until convergence, which is enhanced by using acceleration techniques, and typically takes many hundreds iterations through the modules.

The IEADs as a function of position and phase are obtained using the PCMCM, which calculates the trajectories of charged and neutral species in the gas phase and their intersection with the substrate.²⁷ The PCMCM is a 3v–3d (three velocity components, three dimensions) simulation which integrates ion trajectories in electric fields obtained from the FKM. The PCMCM is executed after the periodic steady state is reached in the remainder of the model. By that time, the continuity, momentum, energy equations for neutrals and ions, continuity equations for electrons, and Maxwell's equations will have been integrated to convergence. The vector components of the electric field are recorded as a function of position and phase over a low frequency rf cycle, $\vec{E}(\vec{r}, \phi)$, which also captures the HF variation. For convenience, the HF and LF are chosen to be multiples of each other. These recordings typically contain hundreds of phase points during the highest frequency period and are recorded on the same spatial mesh as the fluid portion of the model is performed. The fluid module also records cycle-averaged densities of all charged and neutral species, $N_i(\vec{r})$ and source functions for these species. A set of collision probability arrays are also computed, which account for all possible collisions in the reaction mechanism and their energy dependence. In the absence of experimental data or theory, we specify a generic energy dependence for the cross section for elastic collisions of ions of the form $\sigma(\varepsilon) = \sigma_0/(1 + \varepsilon/\varepsilon_0)$. The maximum collision frequency for each PCMCM species, i , over the entire computational domain, ν_{im} , is determined

$$\nu_{im} = \sum_j \nu_{ij}, \quad \nu_{ij} = \max((v\sigma_j(v))_m N_{jm}), \quad (1)$$

where the sum is over collisions j , $(v\sigma_j(v))_m$ is the maximum product of speed and cross section, and N_{jm} is the maximum value of the collision partner in the computational domain. We also define the normalized cumulative collision frequency as

$$\omega_{ij} = \frac{1}{\nu_{im}} \sum_{k=1}^j \nu_{ik}, \quad (2)$$

having range (0,1) which for species i represents the relative probability of each type of collision based on the maximum possible collision frequency in the computation domain over the expected range of energies.

Pseudoparticles representing ions and neutral species are launched from computational cells at times randomly chosen in the rf period in proportion to the source function for each species. The initial velocities are randomly chosen from a Maxwell–Boltzmann distribution having the temperature of that species as computed by the FKM. The randomly chosen time to the next collision is then given by $t_c = t_0 - \nu_{im}^{-1} \ln(1 - r)$, where t_0 is the current time and r is a random number distributed on (0,1). The use of the maximum collision frequency, to be corrected later by through of a null-cross section technique, enables the timestep to be chosen independently of changes in the density of the collision partner, velocity and cross section. Note that a separate random number generator is used for each process requiring random numbers to avoid aliasing effects.

The time step for integrating the trajectory of the particle is determined by the minimum of the randomly chosen time to the next collision, the time required to cross a specific fraction of the computational cell based on the current velocity and acceleration, and a fraction of shortest rf period. In the bulk plasma, the particle is allowed to traverse 0.2–0.5 of a computational cell in any given update. As a surface is approached and the ion enters the presheath and sheath, the fraction of the computational cell that can be traversed in any given timestep is reduced so that the particle energy at the time the surface is intersected is more accurately represented. The equations of motion of the particle are integrated for this timestep, using a second order predictor-corrector method while linearly interpolating the electric fields produced by the FKM as a function of position and phase during the low frequency cycle.

A potential collision occurs when the particle time reaches t_c . At this time, a series of random numbers are chosen to determine whether the collision is null and, if not, what type of collision occurs. The first random number satisfying $\omega_{i,j-1} < r < \omega_{ij}$ selects process j as the possible collision. If for a second random number, $r > v\sigma_j(v)N_j(\vec{r})/\max((v\sigma_j(v))_m N_{jm})$ the collision is null, where $N_j(\vec{r})$ is the actual local density of the collision partner for process j and $v\sigma_j(v)$ is the current value of velocity and cross section. The collision is rejected and called null because the actual collision frequency at location \vec{r} and velocity v is smaller than was used to determine the time to the next collision. In a null collision, the particle is simply not collided. Another time to the next collision is chosen, and the integration of the trajectory is continued. In the case of a real collision, the type of collision determines the energy loss and scattering angle. In the event of an identity changing collision, such as a charge exchange, the trajectories of both the new ion and the new hot neutral are followed.

The velocity components of the particle are recorded as a function of position (radius and height, (\vec{r})) and phase during the rf cycle, ϕ , with each advance of the particle trajectory to produce an ion velocity distribution $f(\vec{v}, \vec{r}, \phi)$ throughout the plasma. The particle's contributions to the distribution are weighted by the time the particle spends in the phase space cell. The $f(\vec{v}, \vec{r}, \phi)$ are then postprocessed after execution of the HPEM to produce IEADs.

We assume that charge exchange collisions are long range. For symmetric charge exchange, the trajectory of the original ion is retained while changing it to a neutral particle. The ion is initialized as a new particle at the site of the collision, with a speed randomly selected from Maxwell–Boltzmann distribution and with randomly selected angular distributions. The temperature of the new ion is that of the former neutral that was computed in the FKM. If the collision is consuming, meaning that the velocity distribution of the product of the collision is not being followed, the particle is deactivated.

The spatial mesh upon which velocity distributions are recorded typically has a finer resolution than that used in the FKM. Due to the potentially large arrays that result from recording phase, energy, position, only a specified portion of the plasma is submeshed to provide $f(\vec{v}, \vec{r}, \phi)$. In this investigation, the focus is on transit of positive ions from the bulk through the presheath to the substrate, and so the submesh is usually restricted to the region shown in Fig. 1. When investigating the sheath and presheath dynamics, the height of the submesh is usually a few centimeters above the wafer. When investigating the transit of ions from the bulk plasma to the substrate, the height of the submesh is 7 cm. The resolution of the submesh is as small as 0.05 cm. The radial limit of the submesh is 16 cm, which extends beyond the edge of the wafer and powered substrate onto the dielectric focus ring. The radial resolution is typically 0.5 cm. For purposes of displaying IEADs, the lowest rf frequency is typically divided into eight phase bins.

Simulations were conducted in Ar/O₂ gas mixtures. The intent of the experimental and computational investigation was to study the transport of argon ions, which have accessible transitions for LIF. Due to details having to do with the design of the reactor and substrate, a Si wafer had to be in place while the LIF measurements were made. The resulting sputtering of the Si wafer and possibly other polymeric materials eventually coated the windows that provided optical access for the diagnostics. So, O₂ was added to the argon in order to prevent contamination of the windows. The reaction mechanism for Ar/O₂ plasma used in the model is discussed in Ref. 28. The IEADs we will discuss are for Ar⁺. Both elastic and charge exchange collisions are included with Ar and O₂. The momentum transfer resulting from Ar⁺ collisions with Ar (the dominant collision partner) is approximately half from elastic collisions and half from charge exchange.²⁹

The IEADs presented in this paper are separately normalized at each spatial and phase point. The raw statistics that are collected in the model are essentially the ion density in a space–velocity volume $d^3\vec{r}d^3\vec{v}$ at different phases. At low frequency, this ion density can vary considerably in these

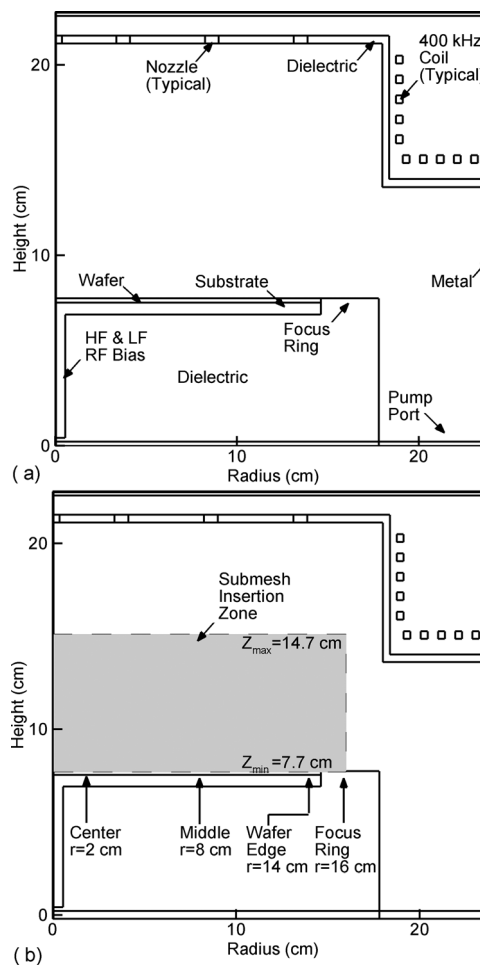


Fig. 1. Properties of the ICP reactor. (a) Schematic showing the wafer on a substrate capacitively powered at LF and HF surrounded by dielectric focus rings. The 10 turn ICP coil surrounds the top of the reactor and is operated at 400 kHz. (b) The submesh insertion zone where IEAD will be analyzed. The radial positions where IEADs will be plotted are labeled.

volumes. Since our emphasis in this paper is on the evolution of the IEADs, we have chosen to separately normalize the IEADs.

III. PLASMA PROPERTIES IN AN ICP REACTOR WITH A SINGLE FREQUENCY RF BIASED SUBSTRATE

The model representation of the ICP reactor used in this study is schematically shown in Fig. 1. The upper portion of the plasma chamber consists of an alumina dome ($\epsilon/\epsilon_0 = 9.0$), 18 cm in radius and 13.5 cm above the wafer, flaring out to an alumina ring having radius of 24 cm. Ten turns of the ICP coil sit on top of the ring and on the vertical surface of the dome. This antenna is driven at 400 kHz. Gas is injected through several nozzles on the top of chamber.

The substrate consists of a dielectric chuck with a center electrical feed to a biased substrate in contact with the wafer. The outer wall of the chamber is grounded. A conductive Si wafer ($\epsilon/\epsilon_0 = 12.5$, $\sigma = 0.01 \Omega^{-1} \text{cm}^{-1}$), 30 cm in diameter, sits in electrical contact with the substrate, which is surrounded with a dielectric focus ring ($\epsilon/\epsilon_0 = 8$, $\sigma = 10^{-6} \Omega^{-1} \text{cm}^{-1}$).

The annular pump port is at the bottom of the computational domain coaxially surrounding the substrate. During execution of the code, the flow rate through the pump port is adjusted to keep the pressure inside the plasma chamber constant.

The base operating conditions are $\text{Ar}/\text{O}_2 = 80/20$ with a flow rate of 50 sccm at a pressure of 2 mTorr. The ICP coils delivered 480 W. The substrate bias is 2 MHz, with a fixed 500 V rf bias with -400 V DC bias. All harmonic voltages are given as amplitudes. In later cases, a HF bias (10 – 60 MHz) is additionally applied to the substrate. The model is capable of self-consistently computing the dc bias and the rf voltage required to deliver a given power. Indeed we found that the dc bias will vary as the bias frequency is changed for a constant voltage or additional frequencies are added to the substrate. Our intent in this paper is to perform side-by-side comparisons of IEADs when changing frequency. As a result, we chose to specify the voltages and dc-biases on the substrate instead of allowing the model to produce these values. This choice allows a more straight forward comparison of IEADs when other parameters are changed.

A. IEADs with a single LF

The reactor scale plasma properties are shown in Fig. 2 for the base case conditions. The peak plasma density is $1.8 \times 10^{11} \text{ cm}^{-3}$ which is sustained by a bulk electron

temperature of $T_e = 4.2\text{--}4.3$ eV. The total positive ion density is $2.5 \times 10^{11} \text{ cm}^{-3}$, yielding a peak electronegativity of 0.28. The maximum gas temperature is 462 K. The inductively coupled coils provide the majority of power deposition to maintain the high-bulk plasma density. The contributions to ionization by the rf bias, either in terms of heating the bulk electrons or producing ionization by secondary electrons, are small. In the middle of the plasma, the ion temperature $T_{\text{ion}} = 0.15$ eV whereas in the near presheath, T_{ion} is at most a few electronvolts. So, in general, we assume $T_{\text{ion}} < T_e$ in the following discussion.

For the base conditions where only a single LF rf bias is applied, $\tau_{\text{ion}}/\tau_{\text{rf}}$ is close to 1 for Ar^+ .^{3,23} The ion transit time τ_{ion} can be estimated by³⁰

$$\tau_{\text{ion}} = 2 \left(\frac{s^2 M_i}{2q \langle V_s \rangle} \right)^{\frac{1}{2}} \left[\left(1 + \frac{k_B T_e}{2q \langle V_s \rangle} \right)^{\frac{1}{2}} - \left(\frac{k_B T_e}{2q \langle V_s \rangle} \right)^{\frac{1}{2}} \right], \quad (3)$$

where s is the sheath thickness, M_i is the ion mass and $\langle V_s \rangle$ is the time-average sheath potential. The electron density n_e at the edge of the sheath is $9.8 \times 10^{10} \text{ cm}^{-3}$ and so the ratio $\tau_{\text{ion}}/\tau_{\text{rf}}$ in this case is estimated to be 0.45.

At 2 mTorr, the mean free path of Ar^+ for charge exchange with Ar and O_2 is ≈ 1.5 cm, which is much larger than the sheath thickness and the vast majority negative ions

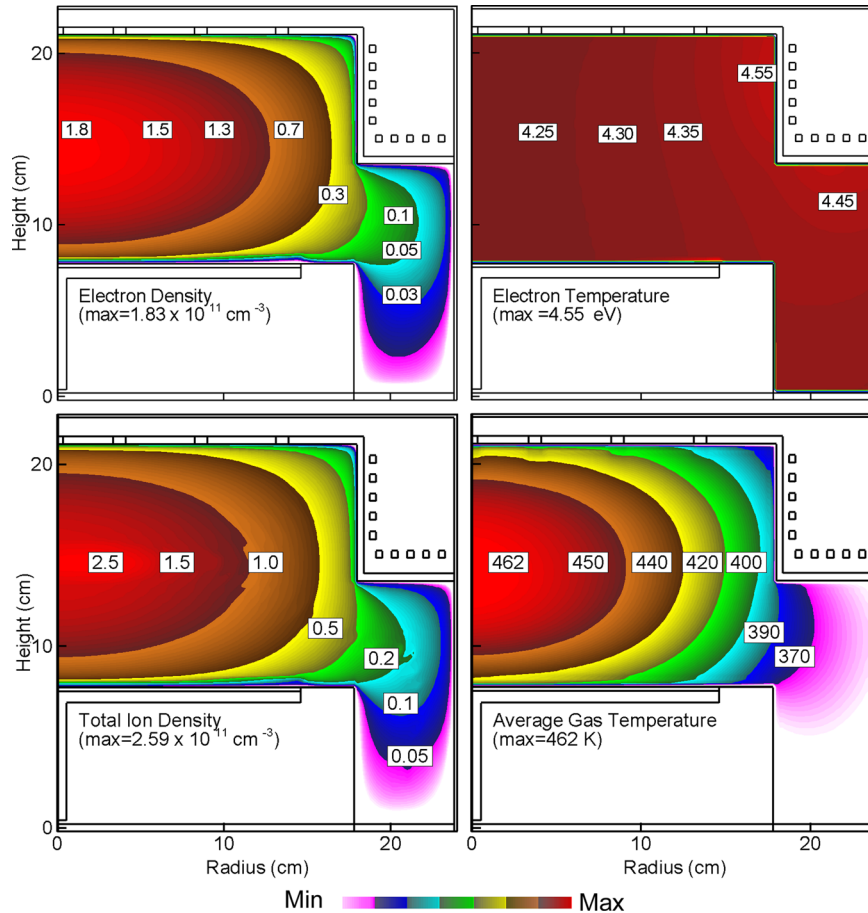


FIG. 2. (Color online) Time averaged plasma properties for the base case conditions ($\text{Ar}/\text{O}_2 = 80/20$, 2 mTorr, 50 sccm, LF = 2 MHz, $V_{\text{LF}} = 500$ V, and DC bias = -400 V). (a) Electron density, (b) electron temperature, (c) total positive ion density, and (d) average gas temperatures. The electron and ion densities are log-scales with contour labels having units of 10^{11} cm^{-3} . The electron temperature and average gas temperature are in linear-scales.

are confined to the bulk plasma. Therefore, the sheath is essentially collisionless. The time averaged IED for Ar^+ at the midradius of the wafer [location labeled *middle* in Fig. 1(b)] as a function of height above the wafer from the bulk plasma through the presheath and sheath is shown in Fig. 3(a). The discontinuities with increase in energy are caused by the discreteness of the mesh used in collecting statistics. The IEDs are separately normalized to unity at each height. The boundary between the presheath and sheath is approximately where the ion energy begins to increase from its nearly constant value in the presheath, and is approximately 4 mm. At a height of 4.5 mm, ions are already well into the presheath, having an average energy of near 10 eV as shown in Fig. 3. In the bulk plasma and near-presheath, the IED is essentially thermal. When ions enter the sheath,

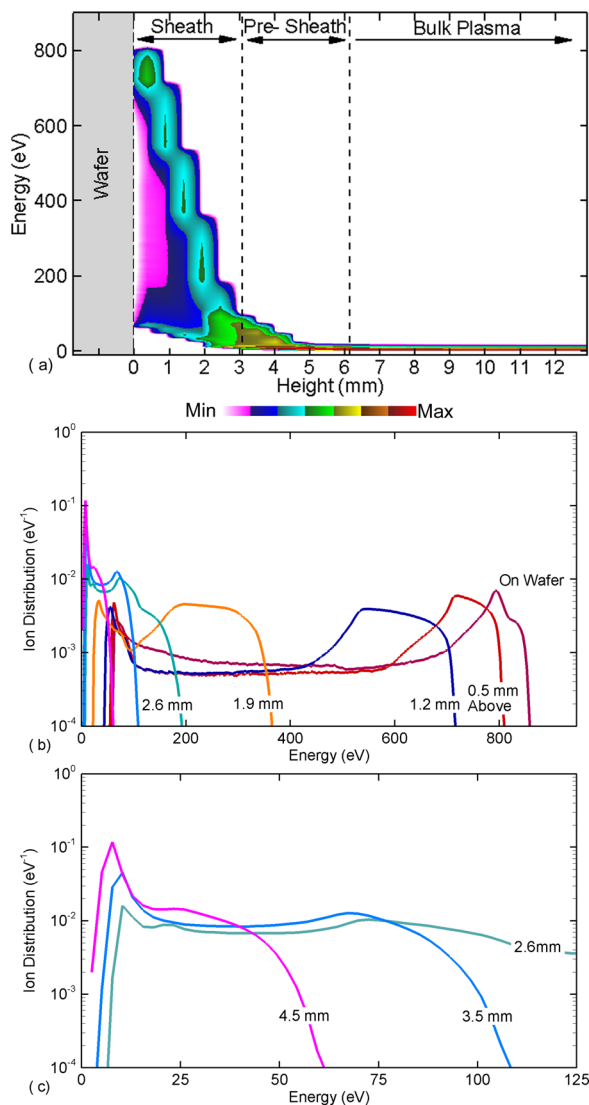


FIG. 3. (Color online) Time averaged IEDs for Ar^+ at the middle of the bulk plasma to sheath region for the base case conditions ($\text{Ar}/\text{O}_2 = 80/20$, 2 mTorr, $\text{LF} = 2$ MHz, $V_{\text{LF}} = 500$ V, DC bias = -400 V). (a) IED from bulk plasma to wafer. The approximate sheath and presheath boundaries are labeled in frame. Discontinuities in energy are caused by the mesh resolution in collecting statistics. (b) IEDs at selected positions over the full energy range. (c) IEDs at 4.5, 3.5, and 2.6 mm above the wafer over a lower range in energy.

the E field in the vertical direction accelerates the ions to higher energy during the cathodic portion of the cycle and forms a bimodal distribution, which can be seen to form starting at about 2 mm above the wafer.

IEADs as a function of height from the bulk plasma (7 cm above the wafer) to the wafer averaged over the rf cycle are shown in Fig. 4. (Similar to the IEDs, all IEADs are separately normalized to unity.) The IEADs from the sheath boundary (4.5 mm height) to the wafer are shown within 15° of the vertical on an energy scale extending to 900 eV. IEADs at greater heights are shown within 90° of the vertical on an energy scale extending to 10 eV. In the bulk plasma, the average ion energy is about 0.15–0.3 eV and the IEAD has essentially an isotropic distribution. The narrowing of the angular distribution due to the anisotropic ambipolar electric field begins at about 4 cm above the wafer, where the axial component of ambipolar electric field, $E_z = -0.29$ V/cm (or $E/N = 725$ Td). At one 1 cm above the wafer, the average energy is about 3 eV, and the distribution has narrowed to 30° , with $E_z = -1.74$ V/cm (or $E/N = 4,350$ Td). Entering the sheath proper is in part indicated by the elevation of the low energy component of the IEAD above thermal, which occurs

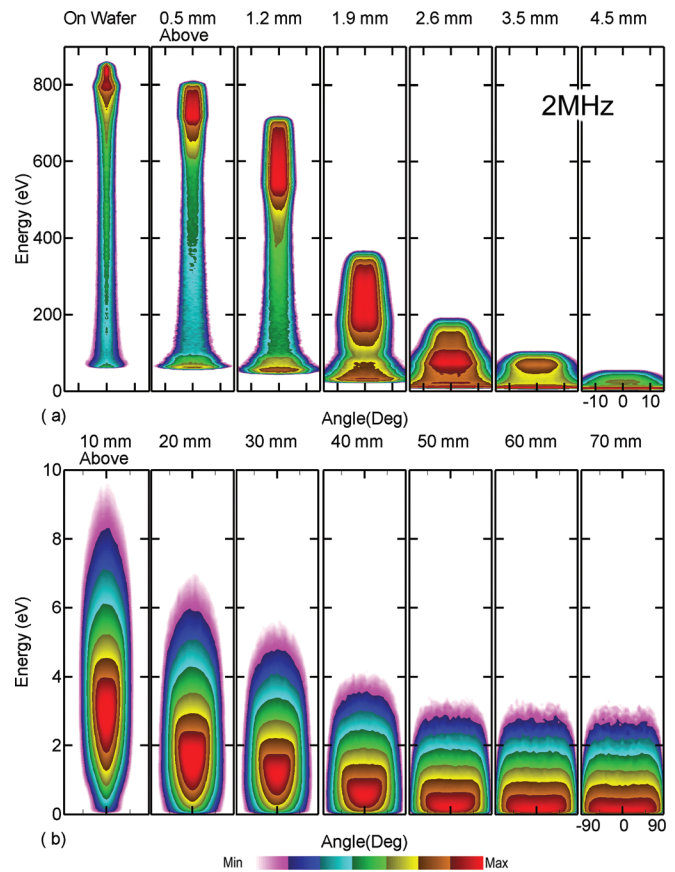


FIG. 4. (Color) Time averaged IEADs for Ar^+ as a function of height above the wafer. IEADs are plotted on a log scale over two decades. (a) IEADs from on wafer to the edge of the presheath for energies up to 900 eV and angles -15 to 15° . (b) IEADs from the presheath into the bulk plasma for energies up to 10 eV and angles -90 to 90° . The operating parameters are the base case ($\text{Ar}/\text{O}_2 = 80/20$, 2 mTorr, $\text{LF} = 2$ MHz, $V_{\text{LF}} = 500$ V, and DC bias = -400 V).

at about 2 mm. It is at this point that the IEAD splits into a bimodal distribution.

As ions transit through the presheath and enter the sheath (between 3.5 and 4.5 mm), the IEDs first uniformly accelerate a few eV before separating into two bimodal peaks, low and high energy. The initial uniform acceleration occurs in that part of the presheath where charge separation is small and there are few cyclic dynamics in the electric field. The fields at this point are still largely ambipolar. Between 3.5 and 2.6 mm, the sheath proper begins with cyclic variation in the electric field, which then produces the bimodal structure, which narrows in angle as the vertical component of the IED begins to dominate. For these conditions, the sheath is essentially collisionless, and so once the ions enter the sheath, their trajectories are ballistic. The width of the IED, ΔE , continues to increase as ions transit through the sheath with the final width being 700 eV prior to striking the wafer. This width can be approximated analytically by^{31,32}

$$\Delta E = \frac{V_{so}\tau_{rf}}{\pi\tau_{ion}}, \quad (4)$$

where V_{so} is the amplitude of the rf sheath voltage drop, which is about 900 V here. Based on our estimate of

$\tau_{rf}/\tau_{ion}=2.2-2.3$, the analytical estimate of ΔE is 570 eV. The differences are largely due to defining where the edge of the sheath precisely sits.

In microelectronics fabrication, it is highly desirable to have both a uniform ion flux and a uniform IEAD to the edge of the wafer so that devices can utilize the entire area of the wafer. (This is termed minimizing *edge exclusion*.) IEADs were separately collected over the center of the wafer (averaging from $r=1-3$ cm), the middle of the wafer ($r=7-9$ cm), the outer portion of the wafer and above the focus ring ($r=15-16$ cm). These IEADs are shown in Fig. 5(a). The decrease in energy over the focus ring is a consequence of the capacitance of the focus ring being smaller than that of the wafer and smaller than that of the sheath. The voltage across the sheath results from voltage division between the capacitance of the sheath, the capacitance of the substrate, and the resistance of the bulk plasma. Since the capacitance of the focus ring is smaller than the wafer, the focus ring charges more rapidly and so removes voltage from the sheath, producing a lower energy IEAD. In the transition region, we see a decrease in peak energy of 30–40 eV and a broadening in angle of the IEAD. This broadening is surprisingly large at higher energy, which is

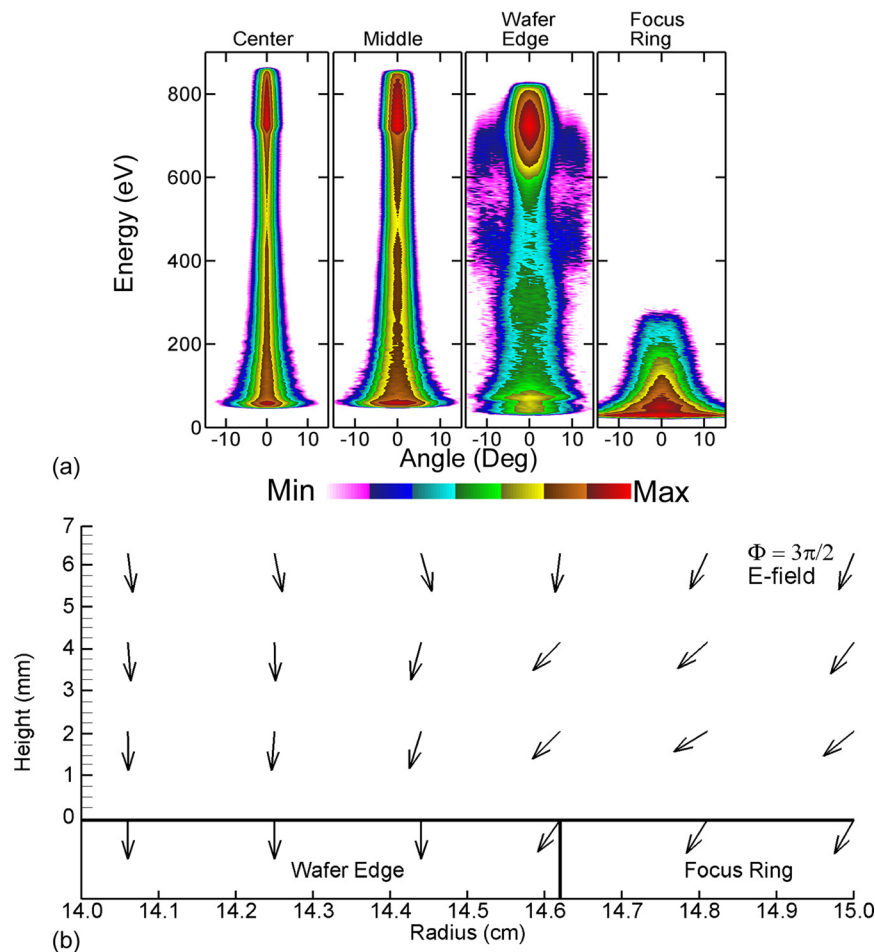


Fig. 5. (Color online) IEADs and electric field vectors as a function of radial position. (a) IEADs Ar^+ 0.5 mm above wafer for the base condition ($\text{Ar}/\text{O}_2 = 80/20$, 2 mTorr, $\text{LF} = 2$ MHz, $V_{\text{LF}} = 500$ V, and DC bias = -400 V). The IEADs are separately collected over the center of the wafer ($r = 1-3$ cm), the middle of the wafer ($r = 7-9$ cm), the edge of the wafer ($r = 13-15$ cm), and the focus ring ($r = 15-16$ cm). The contours span two decades using a log scale. (b) Unit electric field vectors at the edge of the sheath and focus ring at the peak of the cathodic portion of the cycle.

the result of cyclic generation of radial components of the electric field.

Electric field unit vectors as a function of height are shown in Fig. 5(b) averaged over the rf cycle. The electric field transitions from being essentially perpendicular to the wafer to having radial components 3–4 mm from the edge of the wafer. Due to current being collected asymmetrically during the rf period, there are time averaged radial components that point both inwards and outwards as a function of height, which contributes to broadening of the IEAD. Having electric field components that point in only one direction would shift the IEAD to one side. For example, during the anodic portion of the rf cycle, the capacitance of the dielectric focus ring close to the edge of the wafer more rapidly charges than the capacitance of the sheath. Electron current is therefore directed toward the focus ring for only a portion of the cycle.

The development of the IEAD as ions transition from the bulk plasma to the wafer is shown in Fig. 6 for an rf frequency of 2 MHz as a function of height and phase during the period. For these conditions, $\tau_{\text{ion}}/\tau_{\text{rf}} \approx 0.45$. IEADs are shown at eight phases during the rf cycle along each row in the figure, with each row corresponding to a different height above the wafer. The IEADs shown are averaged over that 1/8 of the period. The applied voltage crosses zero from negative to positive at $\phi = 0$, and from positive to negative at $\phi = \pi$. In the right four columns, the rf bias is negative. During this cathodic portion of the cycle, the sheath potential is positive and ions are strongly accelerated during these phases. During this cathodic portion of the cycle, the ions progressively extend to higher energies while narrowing in angle as the wafer is approached.

In the left columns of Fig. 6, the rf bias is positive. During this anodic portion of the cycle, the sheath potential reduces to nearly the floating potential. During this portion of the period, ions retain energies and angular widths akin to that at the edge of the presheath until about 1.5 mm above the wafer. Even with the acceleration that occurs in the last 1 mm above the wafer, the wafer receives predominantly low energy ions of broader spatial extent during the anodic portion of the cycle. IEADs at 3.5 mm above wafer (about 0.5 mm beyond the edge of the presheath) are broad in angle at all phases with only significant acceleration (to about 50 eV) at the peak of the cathodic portion of the cycle. At the peak of the anodic portion of the cycle, the IEADs are nearly unchanged from their shapes in the presheath. Approaching the wafer, the IEADs in the cathodic portion of the cycle extend to higher energy and narrow in angle as the vertical velocity component increases while the horizontal component remains nearly constant.

The width in energy of the IEADs at any given phase is a function of the averaging time, here 1/8 of the cycle—the shorter the averaging time the narrower will be the energy spread. The IEADs during the first and last quarter of the cathodic portion of the cycle appear to be broader in energy since the dV/dt is larger during this averaging period. At the peak of the anodic portion of the cycle, the ions remain at nearly their presheath energies until approaching within

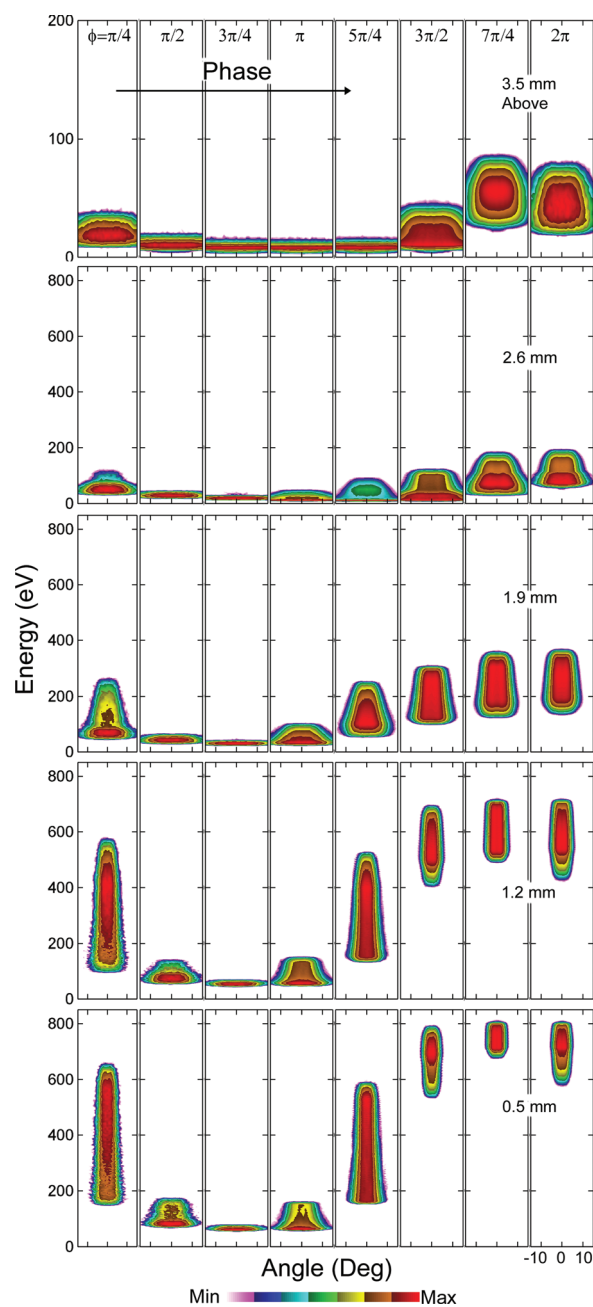


FIG. 6. (Color) IEADs of Ar^+ at the middle of the wafer ($r = 8$ cm) for base condition ($\text{Ar}/\text{O}_2 = 80/20$, 2 mTorr, $\text{LF} = 2$ MHz, $V_{\text{LF}} = 500$ V, and DC bias = -400 V) at different heights above the wafer (top to bottom: 3.5, 2.6, 1.9, 1.2, and 0.5 mm). IEADs are shown averaged over 1/8 of the rf cycle for phases ending at $\phi = \pi/4$ to 2π along each row. The rf bias cross zero (negative to positive) at $\phi = \pi$.

1 mm of the wafer. This implies that the presheath may extend nearly all way to the wafer during certain phases of the rf cycle. The bimodal character of the IEAD obtained for $\tau_{\text{ion}}/\tau_{\text{rf}} \approx 0.45$, is clearly composed of ions that arrive at the substrate with different energies at different phases of the rf cycle.

The IEADs for 2 MHz from 2 to 20 mTorr are shown in Fig. 7. With increasing pressure, the mean free path of the Ar^+ ion decreases. However, even at 20 mTorr, there are few collisions in the sheath. The dominant effect is an increase in the sheath thickness. This increase results from a

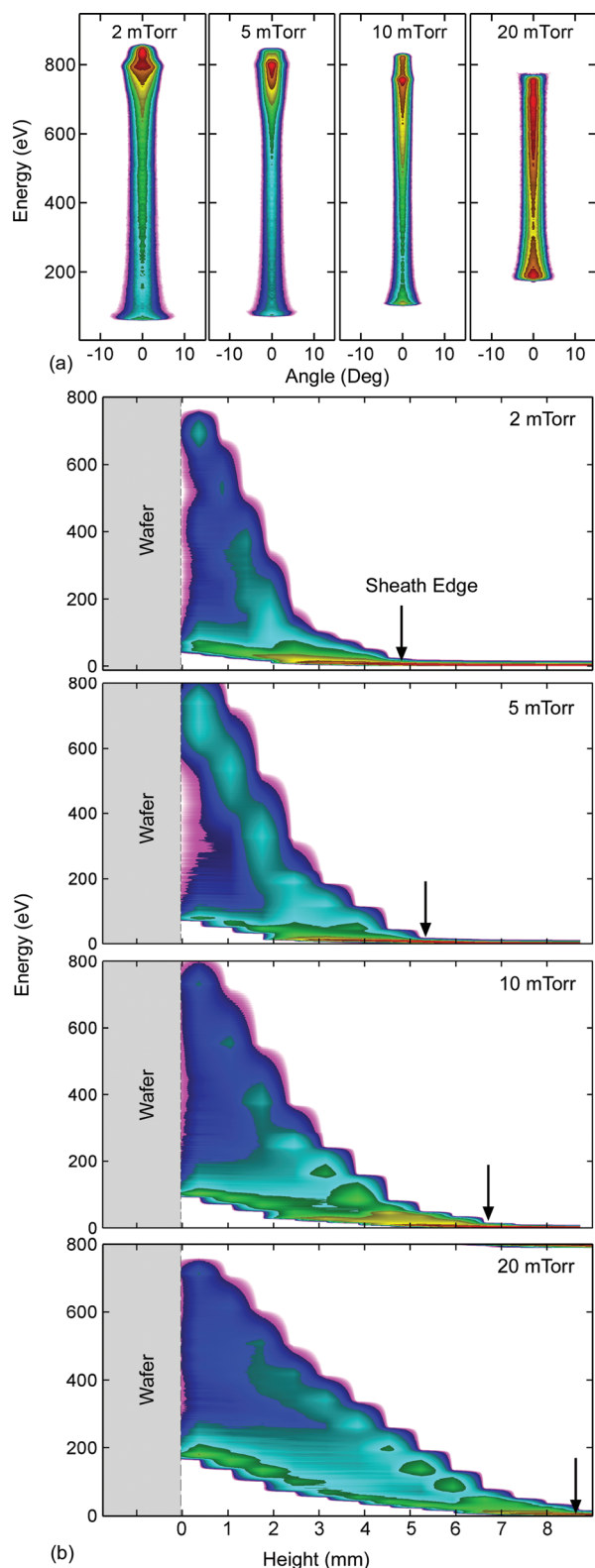


FIG. 7. (Color) Properties of Ar^+ ion transport at the middle of the wafer ($r=8$ cm) for different pressures for otherwise the base case conditions. ($\text{Ar}/\text{O}_2=80/20$, $\text{LF}=2$ MHz, $V_{\text{LF}}=500$ V, and DC bias $=-400$ V). (a) IEADs as a function of pressure (2–20 mTorr). (b) IEDs at the middle of the wafer as a function of height from the bulk plasma to the wafer. With increasing pressure, the lower plasma density increases the thickness of sheath. The thicker sheath increases ion transit times and, coupled with the higher pressure, increases likelihood for collisions.

reduction in the plasma density with increasing pressure for this gas mixture, which then increases the sheath thickness since the bias voltage is constant. With the thicker sheath, the transit time of the ion increases, which narrows the ΔE of the IEAD.

B. IEADs with a single HF

As the substrate bias increases significantly above a few megahertz, $\tau_{\text{ion}}/\tau_{\text{rf}}$ increases above unity, and so the ions sample the oscillations of the sheath over multiple cycles. For sufficiently high frequencies, electron heating from the bias may begin to make a contribution to the plasma density. For example, the electron density is shown in Fig. 8 for rf bias frequencies of 10–60 MHz. (See Fig. 2 for the values at 2 MHz.) For purposes of comparison, the rf bias voltage amplitude (500 V) and DC bias (-400 V) are constant and the same values as for 2 MHz. With electron heating scaling as ω^2 , the power deposition from the rf bias increases from 508 W at 2 MHz (dominantly ion acceleration) to 2370 W at 60 MHz, the latter having electron heating exceeding that due to the inductive coils. As a result, the peak electron density increases with increasing bias frequency from $2.3 \times 10^{11} \text{ cm}^{-3}$ at 10 MHz to $4.8 \times 10^{11} \text{ cm}^{-3}$ at 60 MHz. We note that in practice it would be unusual to use a single 60 MHz frequency at these voltages as the substrate bias in an ICP reactor. This parameterization over frequency using a fixed voltage is for the purpose of investigating scaling laws.

With the increase in frequency, $\tau_{\text{ion}}/\tau_{\text{rf}}$ also increases, and the ions experience more rf cycles before reaching wafer surface. The IEAD and IEDs of Ar^+ onto wafer are shown in Fig. 9 for frequencies of 2–60 MHz. The ΔE of the IEDs progressively decrease and converge on the average sheath potential as the frequency increases due to the increase in $\tau_{\text{ion}}/\tau_{\text{rf}}$. Tsui³³ first demonstrated these trends using PIC simulations of a current-driven collisionless rf plasma sheath. The IEDs from the bulk plasma to and through the sheath for frequencies of 10–60 MHz for otherwise the base-case conditions are shown in Fig. 10. (Note the difference in energy scales for the near-wafer region, 0–4 mm, and the presheath, 4–9 mm) The IEDs in the presheath are not particularly sensitive to frequency. Since the sheath thickness does not appreciably change with frequency (the voltage is fixed and the plasma density changes by less than a factor of 2), the penetration of electric fields from the sheath into the bulk plasma does not significantly change. As a result, there is not a large change in the electric fields in the presheath and the IEDs remain thermal for all frequencies to a height of about 4.5 mm. The structure of the IED suggests that as the frequency increases, the high energy component of the IED converges toward the average sheath potential while the low energy component dissipates. Once the transit time exceeds one rf period as frequency increases, then all of the ions experience high electric fields at some point during the cathodic portion of the cycle. As a result, the low energy component of the IED dissipates.

The IEADs as a function of phase for frequencies of 10–60 MHz at a height of 0.5 mm above the wafer are shown

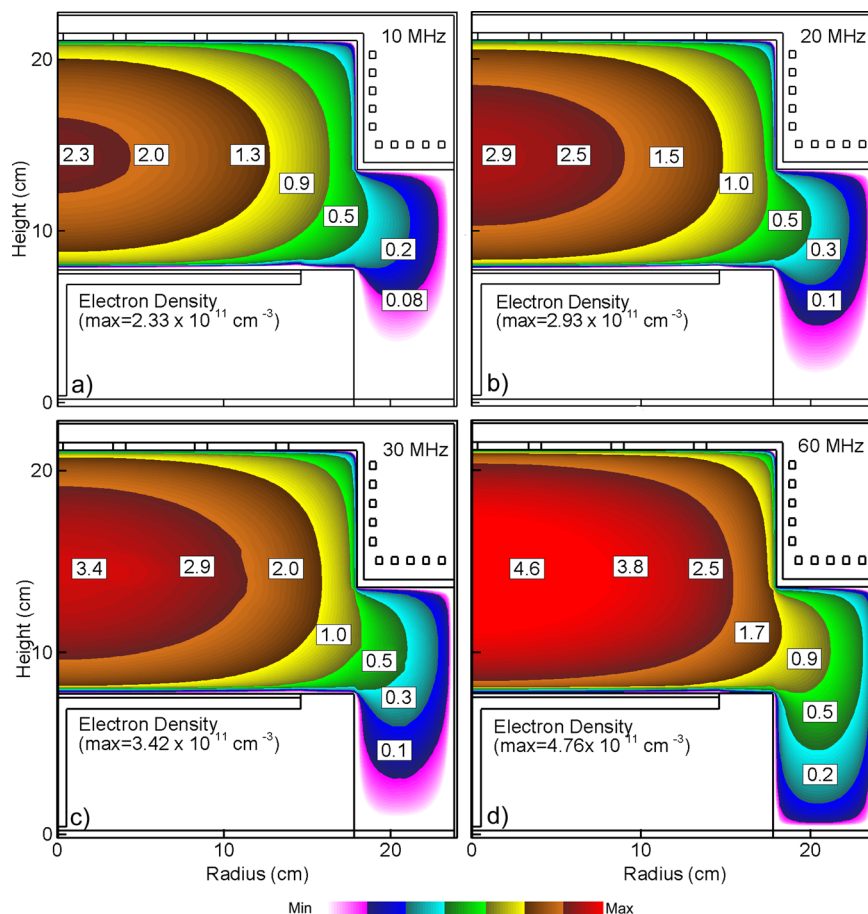


FIG. 8. (Color online) Time averaged electron density for $\text{Ar}/\text{O}_2=80/20$, 2 mTorr, when the HF is varied from (a) 10, (b) 20, (c) 30, and (d) 60 MHz. $V_{\text{HF}}=500$ V, DC bias = -400 V. The maximum electron density, which increases with increasing HF, is noted in each frame with contour labels having units of 10^{11} cm^{-3} .

in Fig. 11. The phases, ϕ , refer separately to each frequency with the voltage crossing zero (negative to positive) at $\phi=0$ and the peak of the cathodic portion of the cycle occurring at $\phi=3\pi/2$. As the frequency and $\tau_{\text{ion}}/\tau_{\text{rf}}$ increase, the phase variation in the IEADs and so the phase variation in ion fluxes to the substrate dissipate. However, even at 30 MHz, there is significant phase modulation—the average ion energy varies by 95 eV over the rf cycle. At 60 MHz, this variation decreases to 50 eV.

Since sinusoidal voltages are specified, nonlinearities in ion and electron transport are revealed in harmonics of the current. As a computational diagnostic, we Fourier analyze the current collected by the substrate. For example, at 10 MHz, approximately 10% of the total current is at harmonics 2–5. At 60 MHz, approximately 6% of the current is at harmonics 2–5.

C. Comparison to experiment

Laser induced fluorescence (LIF) measurements of IVDs were conducted using the experimental setup, techniques and chamber described in detail in Refs. 24 and 25. The LIF measurements produce IVDs (which are converted to IEADs) as a function of height above the wafer, radial position across the wafer, and phase during the rf cycle. The ICP

reactor was run continuously at 480 W at a fill pressure of 0.5 mTorr. This lower pressure was necessary to avoid quenching of the fluorescence by collisions with neutrals. A 2.2 MHz bias was pulsed at 10 Hz and run at an 11% duty cycle. This produces a sufficiently long pulse length that the IEADs are in a quasisteady state. The amplitude of the applied bias was 300 V, with a dc bias of approximately -300 V.

IVD measurements were phase locked and taken during eight phases of the rf cycle. IEADs for these eight phases at a radius of 11 cm (4 cm from the edge of the wafer) are shown in Fig. 12 as a function of height above the wafer, 5.2 mm to 2 mm. (IVDs were not obtained at lower heights due to the low LIF signal.) Ions are shown accelerating from the bulk plasma through the presheath and into the sheath. During the cathodic portion of the cycle (phases $\pi-2\pi$) ions begin accelerating toward the wafer at larger heights above the wafer, a consequence of the thickening of the sheath during the cathodic cycle. During the anodic cycle (phases $0-\pi$), the sheath thins and ions drift toward the wafer to lower heights with IEADs resembling that of the presheath. For $\phi=\pi/2-3\pi/4$, the presheath IEAD is retained to a height of 3.6 mm, and significant acceleration does not occur until a height of 2 mm. These trends are essentially the same as the computed IEADs shown in Fig. 6.

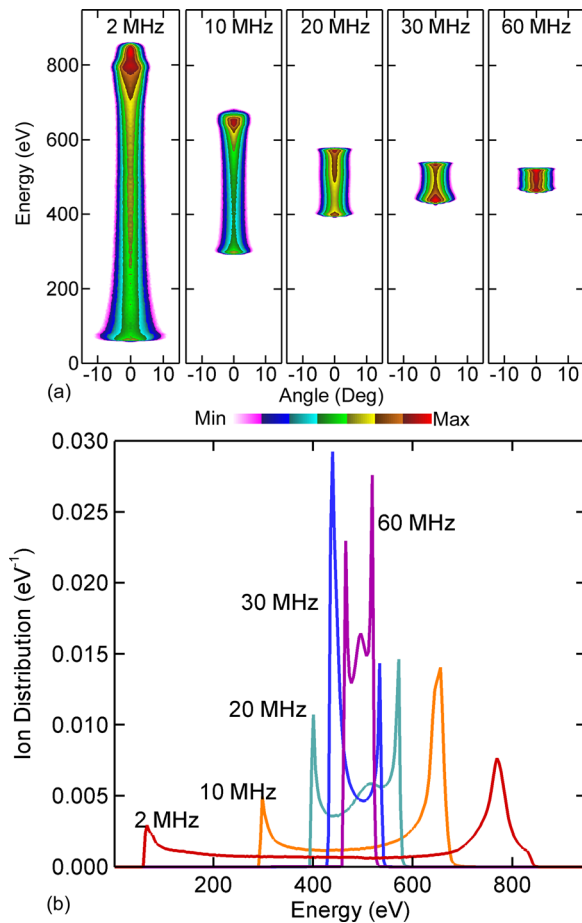


Fig. 9. (Color online) Ar^+ ion properties incident onto the wafer for single frequency biases from 2 to 60 MHz for otherwise the base case conditions ($\text{Ar}/\text{O}_2 = 80/20$, 2 mTorr, $V_{\text{HF}} = 500$ V, and DC bias = -400 V). (a) IEADs and (b) IEDs.

The narrowing of the IEAD when transitioning from the presheath to the sheath is experimentally demonstrated by the results shown in Fig. 13, where time averaged IEADs are shown at several heights above the wafer at a radius of 12.4 cm. Since the LIF measurement of the thermal ion distribution function was power broadened, the perpendicular distribution function widths were scaled so that ions in the bulk plasma bulk are at ambient temperature. The angular distribution narrows as ions traverse the sheath and approach the wafer. The ions at the edge of the presheath may have an angular skew, which is straightened traversing the sheath. Similar trends are also observed in the computed IEADs for a single 2 MHz frequency, as shown in Fig. 4.

IV. DUAL FREQUENCY IEADs

With single frequency excitation, the IEADs, at least for Ar^+ , at high frequencies diminish their dependence on phase during the rf cycle beginning at about 30 MHz. Therefore, to investigate dual-frequency excitation, we focused on combinations of 2 MHz with 10, 20, and 30 MHz. This is also convenient from a computational standpoint since the periods are integral multiples of each other. We first investigated IEADs as a function of phases with equal amplitudes of the

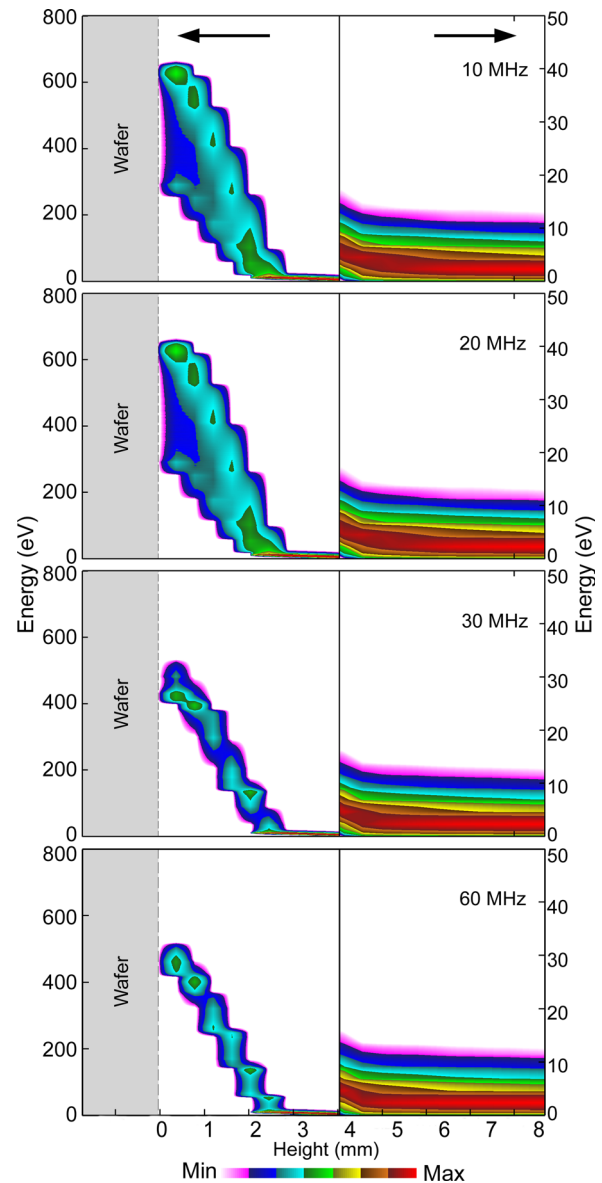


Fig. 10. (Color online) IEDs for Ar^+ as a function of height above the wafer at the middle of the wafer for single frequency biases from 10 to 60 MHz for otherwise the base case conditions ($\text{Ar}/\text{O}_2 = 80/20$, 2 mTorr, $V_{\text{HF}} = 500$ V, and DC bias = -400 V). The left side of each figure is an energy scale up to 800 eV and on the right side on a scale up to 50 eV.

LF and HF biases, 400 V. IEADs for a HF of 10, 20, and 30 MHz are in Figs. 14–16 for 0.5 mm above the wafer. The approximate sheath potential is shown in part (a) of each figure. Rows in part (b) of each figure corresponds to 1/5 of the LF cycle (200 ns), matching the columns shown by dotted lines in part (a). The first two and half rows correspond to the anodic part of the LF cycle (minimum LF sheath potential). The second two and half rows correspond to the cathodic part of the LF cycle (maximum LF sheath potential). For the 10 MHz case, this results in one HF cycle for each row of part (b). For 20 and 30 MHz, each row corresponds to 2 and 3 HF cycles.

The IEADs for 2+10 MHz shown in Fig. 14 reflect the variation previously observed for single frequency biases.

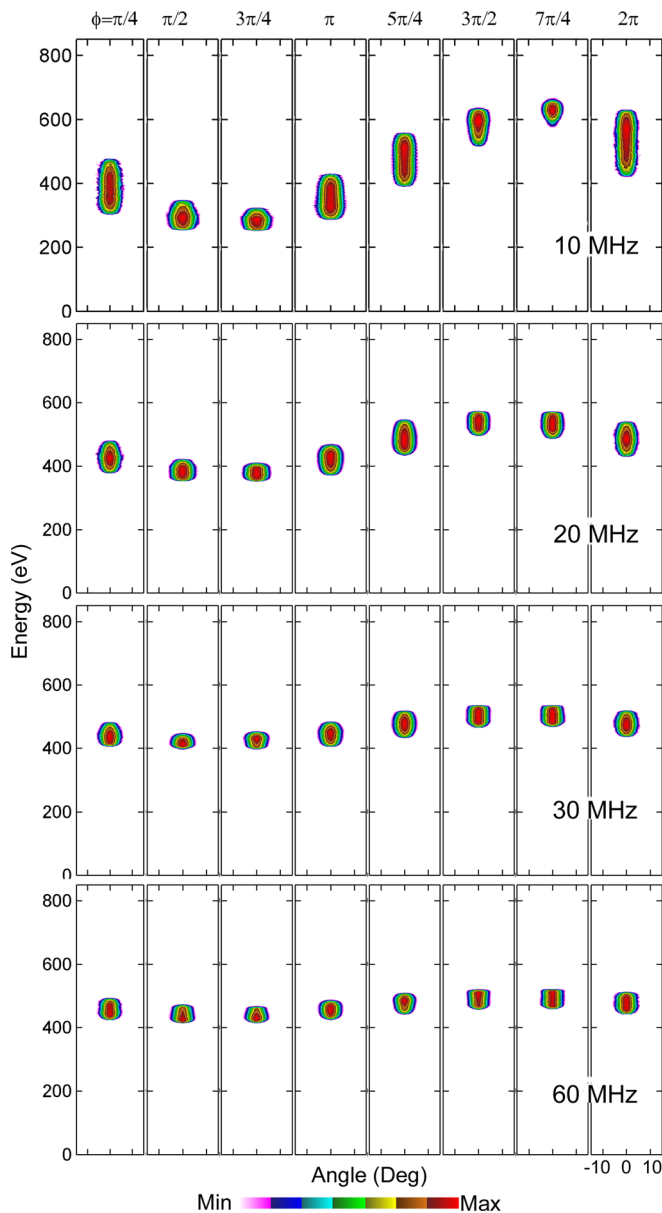


FIG. 11. (Color online) IEADs of Ar^+ at the middle of the wafer ($r = 8$ cm) for frequencies (top to bottom) of 10, 20, 30, and 60 MHz for otherwise the base case condition ($\text{Ar}/\text{O}_2 = 80/20$, 2 mTorr, $V_{\text{HF}} = 500$ V, and DC bias = -400 V). The IEADs are shown 0.5 mm above the wafer averaged over $1/8$ of the rf cycle for phases ending at $\phi = \pi/4$ to 2π along each row. The rf bias cross zero (negative to positive) at $\phi = 0$. With increasing frequency, IEADs become independent of phase.

However, there is a phase delay compared with the instantaneous sheath potential, which can be seen when comparing to the IEADs for single 2 and 10 MHz (Figs. 6 and 11). For the most anodic phases of the LF, there is little phase variation of the IEADs attributable to the HF. There is more phase variation during the cathodic portion of the LF cycle. The maximum variation in the sheath potential by the HF during the anodic phases is the HF amplitude. With only the LF, the sheath potential would be essentially constant during the anodic phase due to the electropositive nature of the plasma. With the amplitudes of the LF and HF being equal, portions of the LF anodic cycle appear to be cathodic due to the HF

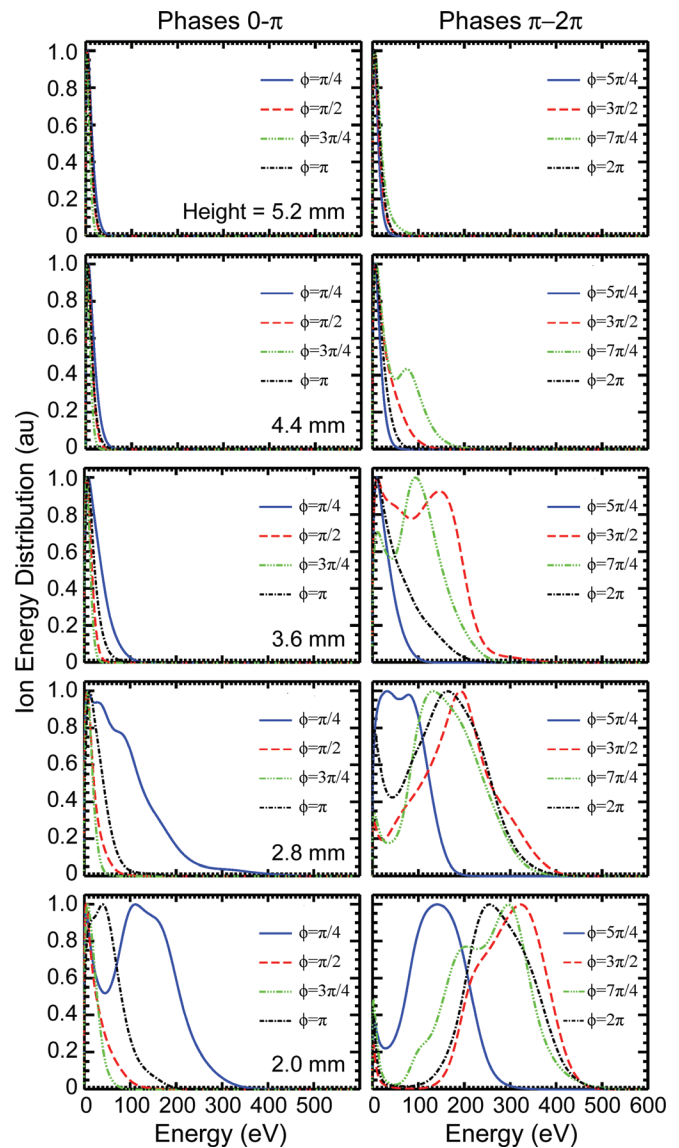


FIG. 12. (Color) Experimentally measured IEDs using LIF for a 2.2 MHz bias at a radius of 11 cm ($\text{Ar}/\text{O}_2 = 80/20$, 0.5 mTorr, $V_{\text{LF}} = 300$ V, and $V_{\text{DC}} = -300$ V). The IEDs are shown at heights above the wafer from 5.2 to 2 mm (top to bottom). The development of the IEDs through the presheath and sheath are shown. During the anodic cycle (phases $0-\pi$), the sheath collapses, and ions drift close to the wafer with IEDs resembling the presheath. During the cathodic cycle (phases $\pi-2\pi$), ions are continuously accelerated through the thicker sheath.

oscillation of the sheath. The oscillation is at most the HF amplitude. In the cathodic phase of the LF, the sheath potential varies by twice the amplitude of the HF. The phase variation resulting from single frequency 10 MHz excitation (see Fig. 11) is significantly larger than phase variation during a 10 MHz cycle for the dual frequency excitation. The maximum energy of IEADs is lower than the maximum instantaneous sheath potential 1200 V (sum of the LF and HF amplitudes plus dc bias), which occurs during the last two 10 MHz cycles. This is likely a consequence of the ion transit time being longer during the short overlap of the cathodic portions of both LF and HF cycles.

IEADs for 2+20 MHz are shown in Fig. 15 where each row in the figure corresponds to 2 HF cycles. The phase

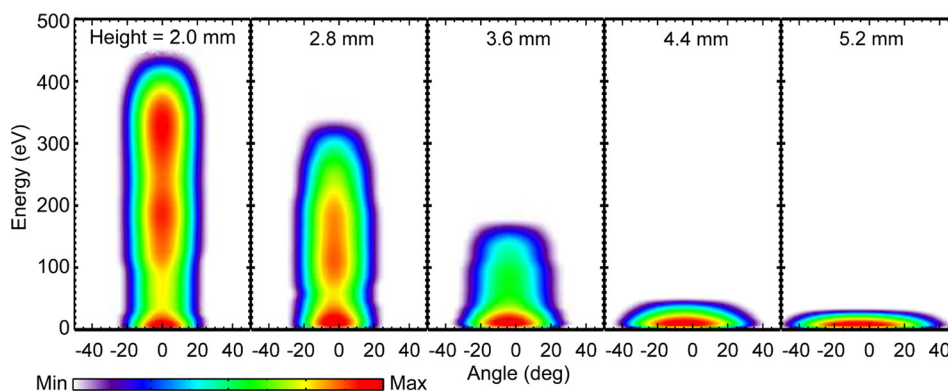


FIG. 13. (Color online) Experimentally measured IEADs using LIF for a 2.2 MHz bias at a radius of 12.4 cm. The IEADs are shown at heights above the wafer from 2 to 5.2 mm (right to left). The narrowing of the IEADs is shown as the ions traverse the presheath and sheath. (Contours are on a log scale over two decades.)

modulation of the IEADs, even on the LF cycle, is suppressed compared to the 2 MHz and 2+10 MHz cases. There is certainly modulation corresponding to the HF but even this modulation is suppressed compared to the single frequency 20 MHz case. This modulation is further suppressed during the anodic portion of the LF cycle. These trends are reinforced by the IEADs for 2+30 MHz shown in Fig. 16. With increasing frequency, the modulation in energy of the IEAD decreases. The oscillation is about 200 eV at 20 MHz and 100 eV at 30 MHz. Assuming the sheath thickness does not change with the change in HF, the ions experience more HF cycles during one LF cycle at 30 MHz, which results in more averaging over the HF cycle. Therefore, the IEADs for 2+30 MHz mainly follow the LF sinusoidal waveform with small a small modulation due to the HF. During the anodic portion of LF, both 2+20 MHz and 2+30 MHz have similar IEADs with a minimum energy of 200 eV, which is about the average of HF amplitude. For the cathodic portion of LF, IEADs for both 2+20 MHz and 2+30 MHz reach maximum energies of 900 eV, which is less than the sum of maximum LF, average HF amplitude, and dc bias. This is likely a consequence of the ions not being able to respond to the HF.

The ion transit time is partially dependent on the sheath thickness, and so the modulation of the IEADs and the apparent phase delays with respect to the maximum sheath potentials may be a consequence of variations in sheath thickness. Wang and Wendt³⁴ found that the sheath thickness is sensitive to the electric field and space charge density at the sheath edge in low pressure high density plasma tools. Experiments performed by Gans *et al.*⁷ and Schulze *et al.*¹⁷ also obtained rapid oscillation of the sheath edge due to coupling of both high and low frequencies. We investigated the relative oscillation in the sheath thickness by examining the modulation in plasma density at the sheath edge, assuming that the sheath thickness will scale with $n_e^{-1/2}$.

The electron density and implied sheath thickness for dual frequency excitation over one LF cycle are shown in Fig. 17. The relative sheath thickness is larger during the last several HF periods in all cases, which corresponds to the cathodic portion of the LF period. The thicker sheath implies

a longer ion crossing time and perhaps explains the phase delay in the IEADs discussed above. The large sheath thickness for 10 MHz at the end of fourth HF cycle is at the coincidence of the peak of the cathodic LF and HF cycles. This thicker sheath may explain why the IEAD fails to reach the maximum sheath potential at this phase (see Fig. 14). The fact that the sheath is thicker during the cathodic portion of the LF for all HF contributes systematically to the phase delay. For 20 and 30 MHz, the variation in sheath thickness is small, and so the phase delay is smaller than at 10 MHz. During the anodic portion of the LF cycle, the sheath thickness has less variation and so the ion transit time has less variation.

The just discussed results were for equal amplitudes of the LF and HF voltages. The IEADs are sensitive functions of the ratio of these amplitudes.^{12,35} For example, time averaged IEADs onto the wafer are shown in Fig. 18 for 2+30 MHz having $V_{HF}/V_{LF} = 0.5, 1.0,$ and 2.0 . The time averaged IEADs in all cases show multi-peaks with the addition of the HF bias. The low ratio of V_{HF}/V_{LF} produces an IEAD similar to that for a single frequency 2 MHz as the LF voltage dominates the sheath potential, and the ions have difficulty responding to the HF. Nevertheless, adding HF does enable the ions to experience higher electric fields and so does narrow the angular spread compared with single frequency case. In all cases, the average energy of the IEAD corresponds to the average sheath potential over the LF cycles.

The multiple peaks observed in the time averaged IEADs onto the wafer come from ion dynamics occurring at different phases. These trends are shown in Figs. 19 and 20, where IEADs are plotted at 0.5 mm above the wafer for 2+30 MHz with $V_{HF}/V_{LF} = 0.5$ (Fig. 19) and $V_{HF}/V_{LF} = 2.0$ (Fig. 20). IEADs follow the instantaneous 2 MHz sheath potential with the addition of the average 30 MHz contribution to the sheath potential. In the $V_{HF}/V_{LF} = 2.0$ case (Fig. 20), the average sheath potential is larger during the anodic portion of the LF cycle, thereby elevating the IEADs to higher energy though in a phase dependent manner. This produces modulation in the IEAD during the anodic portion of the cycle that is preserved as peaks in the on-wafer IEADs.

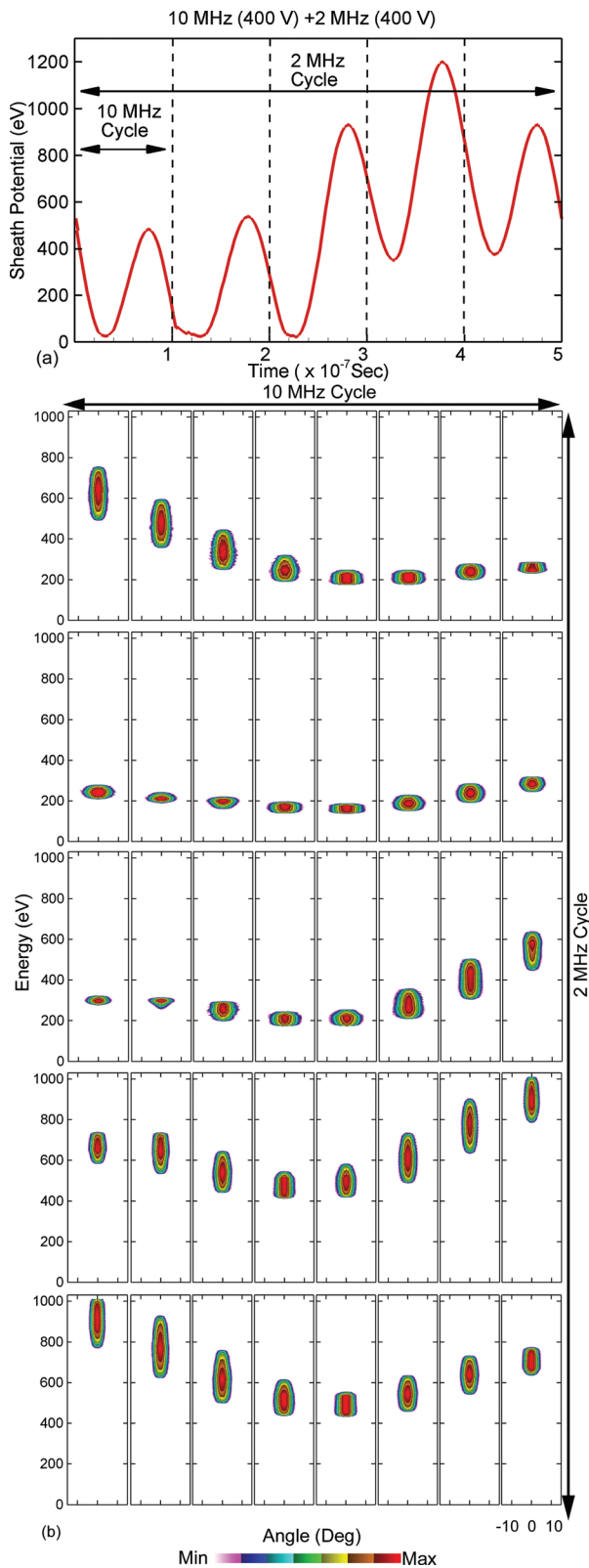


FIG. 14. (Color) IEADs for a two frequency rf bias having LF=2 MHz ($V_{LF}=400$ V) and HF=10 MHz ($V_{HF}=400$ V) with the DC bias = -400 V, (a) Amplitude of the sheath potential during one 2 MHz period. The dashed lines mark the 10 MHz periods, and each column corresponds to each row below. (b) IEADs for Ar^+ at the middle of the wafer for the entire 2 MHz cycle at a height of 0.5 mm. The IEAD for $\phi=0$ for the LF is in the top left corner. Each row of IEADs corresponds to a single 10 MHz cycle.

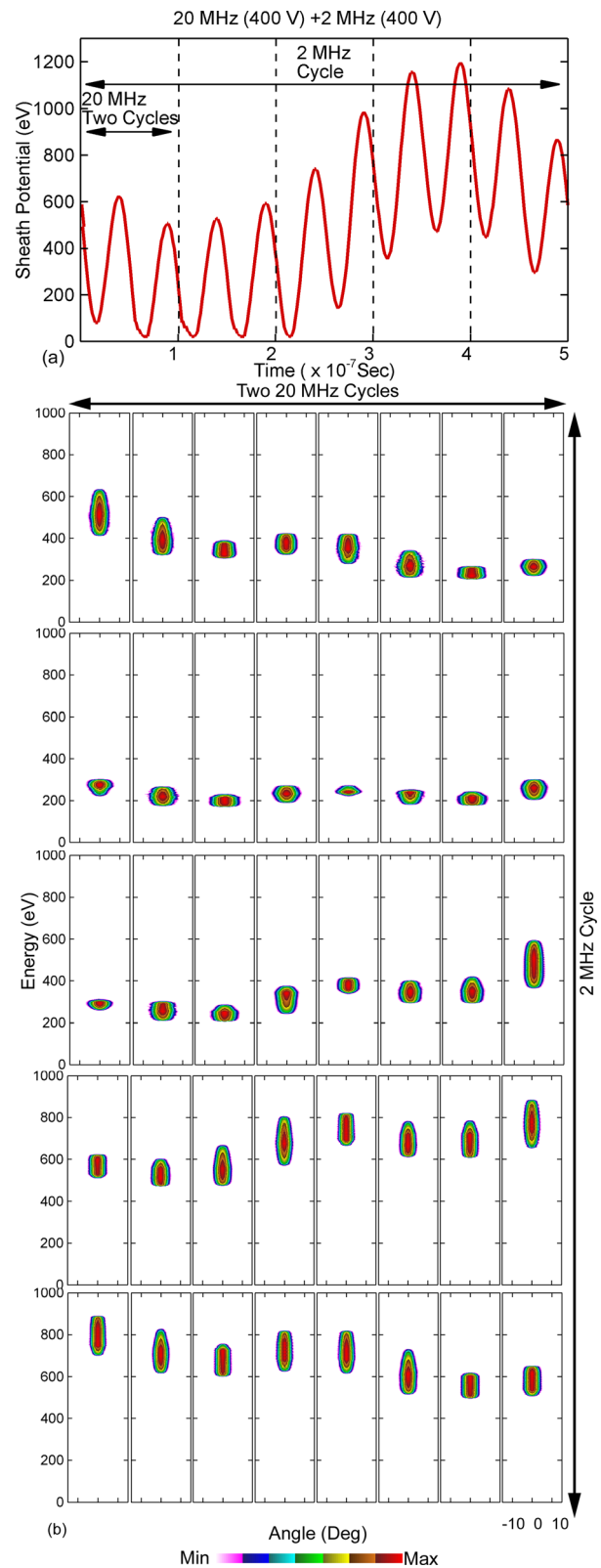


FIG. 15. (Color online) IEADs for a two frequency rf biases having LF=2 MHz ($V_{LF}=400$ V) and HF=20 MHz ($V_{HF}=400$ V) with the DC bias = -400 V. (a) Amplitude of the sheath potential during one 2 MHz period. The dashed lines mark two 20 MHz periods, and each column corresponds to each row below. (b) IEADs for Ar^+ at the middle of the wafer for the entire 2 MHz cycle at a height of 0.5 mm. The IEAD for $\phi=0$ for the LF is in the top left corner. Each row of IEADs corresponds to two 20 MHz cycles.

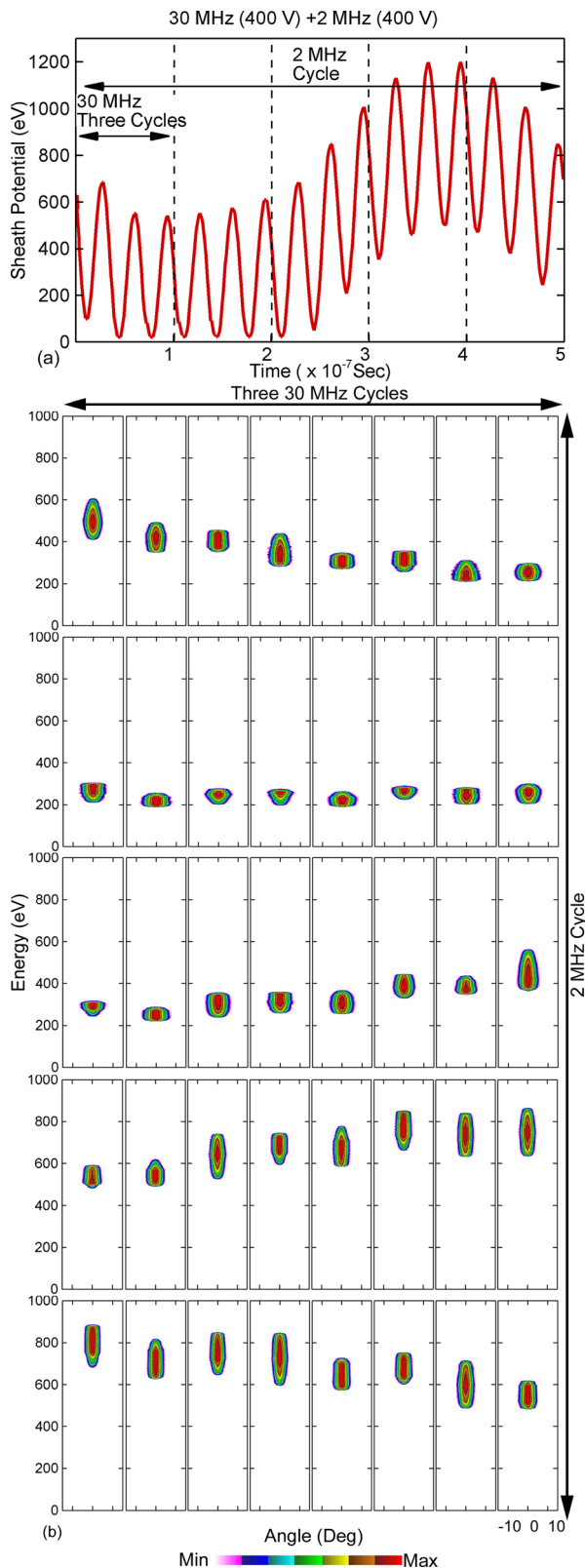


FIG. 16. (Color online) IEADs for a two frequency rf bias having LF=2 MHz ($V_{LF}=400$ V) and HF=30 MHz ($V_{HF}=400$ V) with the DC bias = -400 V. (a) Amplitude of the sheath potential during one 2 MHz period. The dashed lines mark three 30 MHz periods, and each column corresponds to each row below. (b) IEADs for Ar^+ at the middle of the wafer for the entire 2 MHz cycle at a height of 0.5 mm. The IEAD for $\phi=0$ for the LF is in the top left corner. Each row of IEADs corresponds to three 30 MHz cycles.

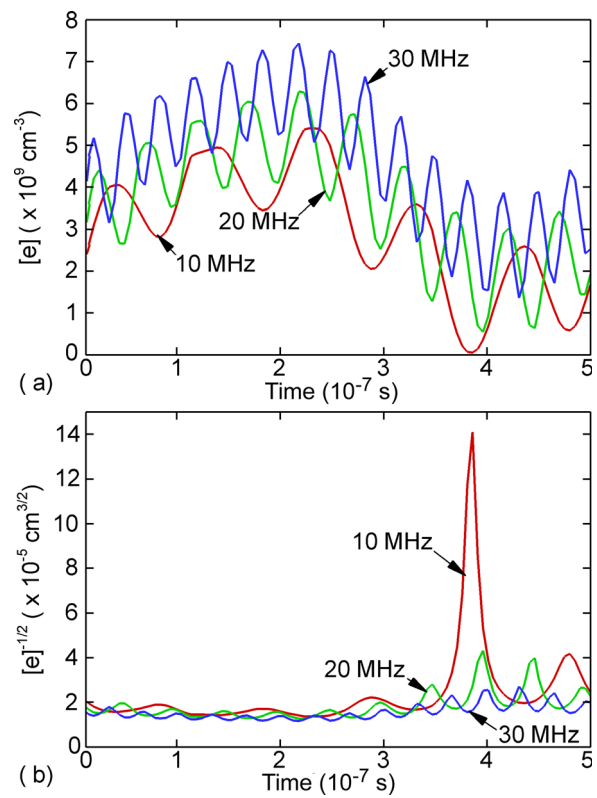


FIG. 17. (Color online) Sheath properties for LF=2 MHz ($V_{LF}=400$ V and HF=10, 20 and 30 MHz ($V_{HF}=400$ V) with the DC bias = -400 V. (a) Electron density at 1 mm above the middle of the wafer during one LF period. The increase of the HF produces a higher electron density. (b) Implied change in sheath thickness assuming a scaling of $[e]^{-0.5}$. The sheath thickness varies within the rf period.

There is more modulation during the anodic LF cycle as the HF dominates the sheath dynamics. For the $V_{HF}/V_{LF}=0.5$ case, the sheath potential is lower in the anodic phases of LF cycle, which results in a broader IEAD.

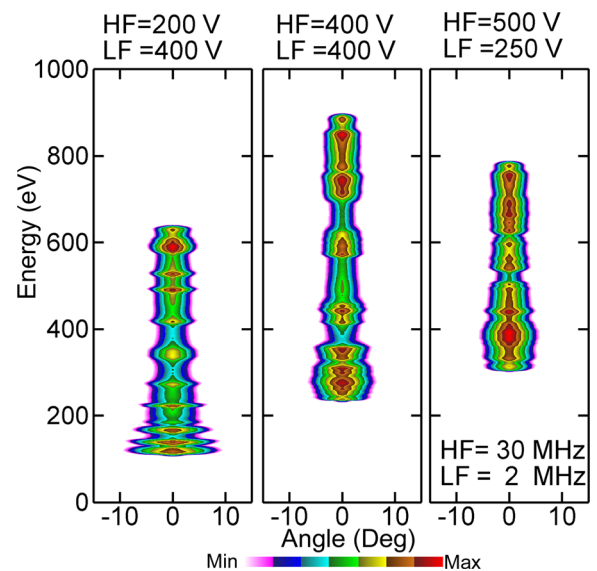


FIG. 18. (Color online) IEADs of Ar^+ onto wafer for dual frequency excitation with LF=2 MHz and HF=30 MHz. The ratio of $V_{HF}/V_{LF}=0.5, 1.0,$ and 2.0 from left to right.

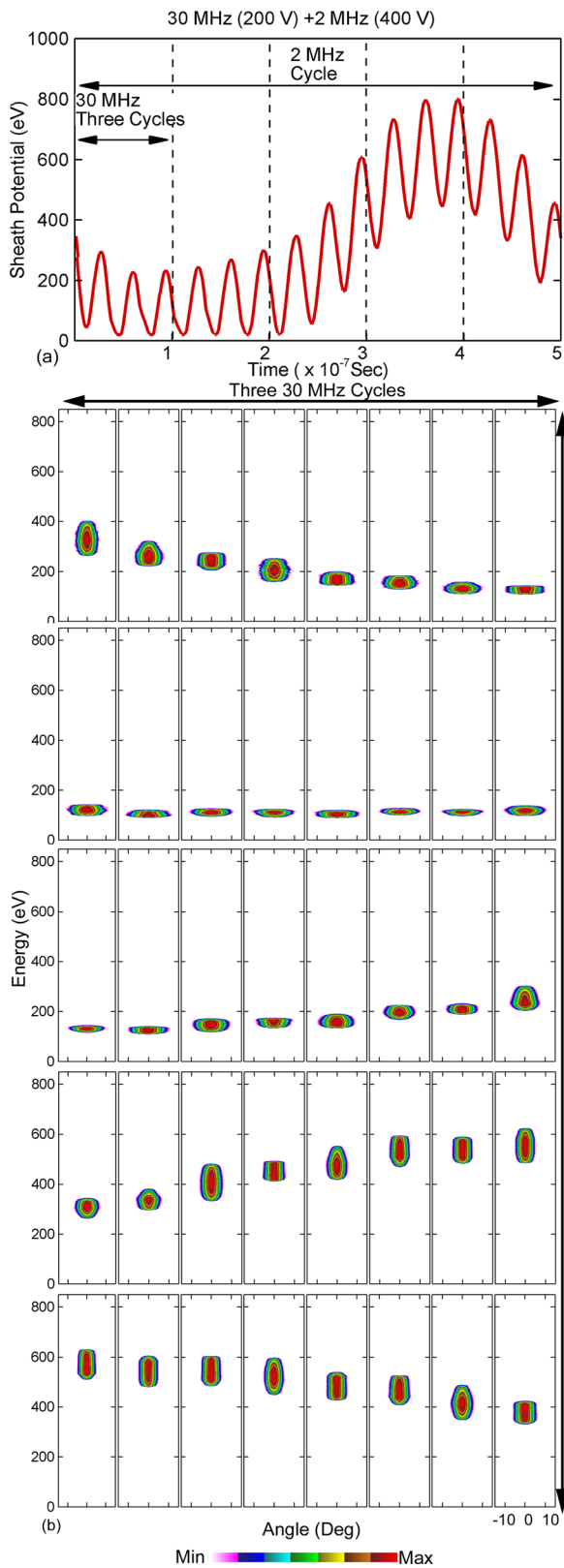


FIG. 19. (Color online) IEADs for a two frequency rf bias having LF = 2 MHz ($V_{LF} = 400$ V) and HF = 30 MHz ($V_{HF} = 200$ V), that is, $V_{HF}/V_{LF} = 0.5$, with the DC bias = -400 V. (a) Amplitude of the sheath potential during one 2 MHz period. The dashed lines mark three 30 MHz periods, and each column corresponds to each row below. (b) IEADs for Ar^+ at the middle of the wafer for the entire 2 MHz cycle at a height of 0.5 mm. The IEAD for $\phi = 0$ for the LF is in the top left corner. Each row of IEADs corresponds to three 30 MHz cycles.

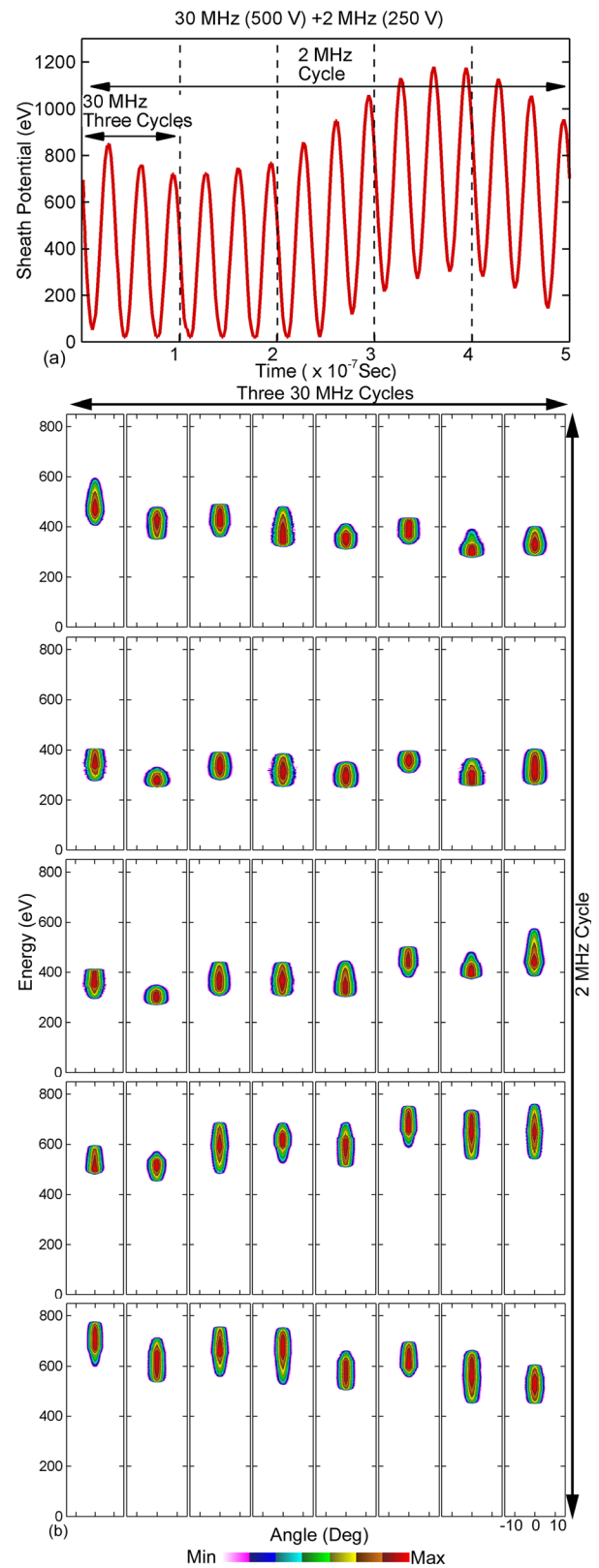


FIG. 20. (Color online) IEADs for a two frequency rf bias having LF = 2 MHz ($V_{LF} = 250$ V) and HF = 30 MHz ($V_{HF} = 500$ V), that is, $V_{HF}/V_{LF} = 2.0$, with the DC bias = -400 V. (a) Amplitude of the sheath potential during one 2 MHz period. The dashed lines mark three 30 MHz periods, and each column corresponds to each row below. (b) IEADs for Ar^+ at the middle of the wafer for the entire 2 MHz cycle at a height of 0.5 mm. The IEAD for $\phi = 0$ for the LF is in the top left corner. Each row of IEADs corresponds to three 30 MHz cycles.

V. CONCLUSION

The properties of IEADs as ions transit from the bulk plasma through the presheath and sheath in an industrial ICP reactor with a capacitively coupled substrate bias were computationally investigated for single and dual frequency excitation. We found that there is significant phase variation in the IEADs as a function of height up to frequencies as high as 30 MHz for Ar⁺ ions. At low frequencies, the presheath extends nearly to within 1 mm of the wafer during the anodic portion of the cycle and so the IEADs remain low energy and broad in angle during this portion of the cycle. As a result, the bimodal IEAD contains a low energy, broad angular component arriving during the anodic portion of the cycle and a high energy, narrow angular component arriving during the cathodic portion of the phases. When increasing frequency, the bimodal distribution is known to transit into a single peak. The transition appears to occur by first losing the low energy component. This is due to the presheath no longer extending as close to the wafer during the anodic portion of the cycle. These trends are corroborated by LIF measurements of IVDs as ions transit the sheath. With dual-frequency excitation, time averaged IEADs incident onto the wafer have multiple peaks. These peaks can be correlated with phase dependent energy oscillations and phase delays due to the interference between the LF and HF, and perhaps some phase dependent thickening of the sheath. The ratio of the voltage amplitudes of the LF and HF sources is an important parameter to control these phase variations.

ACKNOWLEDGMENTS

This work was supported by National Science Foundation (Grant No. 1004203), the Semiconductor Research Corp., and the Department of Energy Office of Fusion Energy Science (Grant No. DE-SC0001939).

¹E. Kawamura, V. Vahedi, M. A. Lieberman, and C. K. Birdsall, *Plasma Sources Sci. Technol.* **8**, R45 (1999).

²W. J. Goedheer, *Plasma Sources Sci. Technol.* **9**, 507 (2000).

- ³V. Georgieva, A. Bogaerts, and R. Gijbels, *J. Appl. Phys.* **94**, 3748 (2003).
- ⁴T. Kitajima, Y. Takeo, and T. Makabe, *J. Vac. Sci. Technol. A* **17**, 2510 (1999).
- ⁵V. Georgieva and A. Bogaerts, *J. Appl. Phys.* **98**, 023308 (2005).
- ⁶T. Kitajima, Y. Takeo, Z. Lj. Petrović, and T. Makabe, *Appl. Phys. Lett.* **77**, 489 (2000).
- ⁷T. Gans, J. Schulze, D. O'Connell, U. Czarnetzki, R. Faulkner, A. R. Ellingboe, and M. M. Turner, *Appl. Phys. Lett.* **89**, 261502 (2006).
- ⁸J. P. Booth, G. Curley, D. Marić, and P. Chabert, *Plasma Source Sci. Technol.* **19**, 015005 (2010).
- ⁹M. Olevanov, O. Proshina, T. Rakhimova, and D. Voloshin, *Phys. Rev. E* **78**, 026404 (2008).
- ¹⁰S.-B. Wang and A. E. Wendt, *J. Appl. Phys.* **88**, 643 (2000).
- ¹¹Y. Zhang, J. Liu, Y. Liu, and X. Wang, *Phys. Plasmas* **11**, 3840 (2004).
- ¹²J. K. Lee, O. V. Manuilenko, N. Y. Babaeva, H. C. Kim, and J. W. Shon, *Plasma Sources Sci. Technol.* **14**, 89 (2005).
- ¹³T. Yagisawa, K. Maeshiga, T. Shimada, and T. Makabe, *IEEE Trans. Plasma Sci.* **32**, 90 (2004).
- ¹⁴K. Maeshige, G. Washio, T. Yagisawa, and T. Makabe, *J. Appl. Phys.* **91**, 9494 (2002).
- ¹⁵R. Silapunt, A. E. Wendt, and K. H. R. Kirmse, *J. Vac. Sci. Technol. B.* **25**, 1882 (2007).
- ¹⁶A. Metze, D. W. Ernie, and H. J. Oskam, *J. Appl. Phys.* **65**, 993 (1989).
- ¹⁷J. Schulze, T. Gans, D. O'Connell, U. Czarnetzki, A. R. Ellingboe, and M. M. Turner, *J. Phys. D: Appl. Phys.* **40**, 7008 (2007).
- ¹⁸M. A. Sobolewski, J. K. Olthoff, and Y. Wang, *J. Appl. Phys.* **85**, 3966 (1999).
- ¹⁹S. Banna *et al.*, *Trans. Plasma Sci.* **37**, 1730 (2009).
- ²⁰B. K. Woodcock, J. R. Busby, T. G. M. Freegarde, and G. Hancock, *J. Appl. Phys.* **81**, 5945 (1997).
- ²¹X. Wang and N. Hershkowitz, *Phys. Plasmas* **13**, 053503 (2006).
- ²²G. A. Hebner, *J. Appl. Phys.* **80**, 2624 (1996).
- ²³I. A. Biloiu, X. Sun, and E. Scime, *Rev. Sci. Instrum.* **77**, 10F301 (2006).
- ²⁴B. Jacobs, W. Gekelman, and P. Pribyl, *Appl. Phys. Lett.* **91**, 161505 (2007).
- ²⁵B. Jacobs, W. Gekelman, P. Pribyl, and M. Barnes, *Phys. Plasmas* **18**, 053503 (2011).
- ²⁶M. J. Kushner, *J. Phys. D: Appl. Phys.* **42**, 194013 (2009).
- ²⁷A. Agarwal and M. J. Kushner, *J. Vac. Sci. Technol. A* **27**, 37 (2009).
- ²⁸S. Rauf and M. J. Kushner, *J. Appl. Phys.* **82**, 2805 (1997).
- ²⁹A. V. Phelps, *J. Phys. Chem. Ref. Data* **20**, 557 (1991).
- ³⁰M. S. Barnes, J. C. Forster, and J. H. Keller, *IEEE Trans. Plasma Sci.* **19**, 240 (1991).
- ³¹B. Jacobs, Doctor of Philosophy in Physics Dissertation, UCLA (2010).
- ³²T. Panagopoulos and D. J. Economou, *J. Appl. Phys.* **85**, 3435 (1999).
- ³³R. T. C. Tsui, *Phys. Rev.* **168**, 107 (1968).
- ³⁴S.-B. Wang and A. E. Wendt, *IEEE Trans. Plasma Sci.* **27**, 1358 (1999).
- ³⁵G. Wakayama and K. Nanbu, *IEEE Trans. Plasma Sci.* **31**, 638 (2003).